

Constraining the evolution of [CII] intensity through the end stages of reionization

Hamsa Padmanabhan^{1,2*}

¹Canadian Institute for Theoretical Astrophysics, 60 St. George St, Toronto, Ontario M5S 3H8, Canada

²Institute for Particle Physics and Astrophysics, ETH Zurich, Wolfgang-Pauli-Strasse 27, CH-8093 Zürich, Switzerland

Accepted —. Received —; in original form —

ABSTRACT

We combine available constraints on the local [CII] 158 μm line luminosity function from galaxy observations (Hemmati et al. 2017), with the evolution of the star-formation rate density and the recent [CII] intensity mapping measurement in Pullen et al. (2018, assuming detection), to derive the evolution of the [CII] luminosity - halo mass relation over $z \sim 0 - 6$. We develop convenient fitting forms for the evolution of the [CII] luminosity - halo mass relation, and forecast constraints on the [CII] intensity mapping power spectrum and its associated uncertainty across redshifts. We predict the sensitivities to detect the power spectrum for upcoming PIXIE-, STARFIRE-, EXCLAIM-, CONCERTO-, TIME- and CCAT-p-like surveys, as well as possible future intensity mapping observations with the ALMA facility.

Key words: cosmology:observations – radio lines:galaxies – cosmology:theory

1 INTRODUCTION

Intensity mapping of atomic and molecular lines has emerged as a novel approach towards the study of large scale structure. Having been widely used for studying neutral hydrogen (e.g., Chang et al. 2010; Masui et al. 2013; Switzer et al. 2013; Anderson et al. 2018), it has now emerged as an exciting potential probe of various species of ionized and molecular gas in the post-reionization universe and recently, also the epoch of reionization (e.g., Gong et al. 2012; Lidz & Taylor 2016; Mashian et al. 2015; Dumitru et al. 2018). Since intensity mapping is sensitive to the total emission from all galaxies, it does not suffer from the magnitude cuts which are imposed on galaxy luminosity functions, and may thus offer a powerful tracer of the faintest galaxies thought to be responsible for reionization. Allowing for the low luminosity end of the galaxy population to be mapped effectively also makes this a complementary technique to galaxy surveys. In addition, cross-correlating various intensity mapping datasets provides a possible way of probing the large scale structure (e.g., Gong et al. 2012).

The fine structure line of ionized carbon ([CII]), with a rest wavelength 157.7 μm is thought to be an important tracer of the interstellar medium at the late stages of reionization (e.g., Gong et al. 2012; Serra et al. 2016; Li et al. 2016; Crites et al. 2017) due to its close association with star forming galaxies. This line arises due to a hyperfine transition between the $^2P_{3/2}$ and $^2P_{1/2}$ states of singly ionized carbon. CII is the dominant coolant in the interstellar medium, and with an ionization potential of 11.6 eV, the emission line is associated both with neutral and ionized hydrogen regions. The continuum foregrounds associated with [CII] emission

are also smaller than for other emission lines. Above redshifts of about 0.6, the [CII] line becomes the brightest in the far-infrared and sub-millimetre part of galaxy spectra. It is known that the [CII] emission is closely connected to the star formation rate by a power law relation (De Looze et al. 2014) and thus offers constraints on the sources responsible for reionization. [CII] intensity mapping surveys also have the potential to constrain cosmology and models of inflation through measurements of primordial non-Gaussianities (e.g., Fonseca et al. 2018; Moradinezhad Dizgah & Keating 2018).

There are several planned experiments that aim to place constraints on the integrated intensity of [CII] over the epoch of reionization, including (i) the Cerro Chajnantor Atacama Telescope (CCAT-prime; Parshley et al. 2018)¹ which plans to trace [CII] over $z \sim 5 - 8$, probing the late stages of reionization, (ii) the Tomographic Intensity Mapping Experiment (TIME; e.g., Crites et al. 2014, 2017) and (iii) the CarbON CII line in post-rEionization and ReionizaTiOn (CONCERTO; Serra et al. 2016; Lagache 2018) experiment² which plans to observe the evolution of CII over $z \sim 4.5 - 8.5$. Above $z \sim 4$, the [CII] line redshifts into the millimetre wavelengths, where the Atacama Large Millimetre Array (ALMA) facility can make observations in the single dish mode; the ALMA bands 7 and 8 enable [CII] emission observations from $z \sim 2.8 - 5$.

Much of the present data available in the context of [CII] observations at the epoch of reionization relies on individual galaxies, imaged e.g. with the ALMA telescope (Capak et al. 2015; Smit et al. 2018; Pentericci et al. 2016). On the other hand, local galaxies

* Email: hamsa@cita.utoronto.ca

¹ http://www.ccatobservatory.org/docs/ccat-technical-memos/ccatp_im_v2.pdf

² <https://people.lam.fr/lagache.guilaine/CONCERTO.html>

have been used to compute the [CII] luminosity function at $z \sim 0$ (Hemmati et al. 2017). At redshifts $z \sim 2$, observations of [CII] offer interesting prospects towards constraining the peak of the star-formation rate density of the universe, however, these wavelengths are not accessible from the ground. Nevertheless, there are interesting prospects for balloon-based observations of [CII] at intermediate redshifts, $z \sim 1 - 1.5$ (Uzgil et al. 2014) as well as from upcoming studies of CMB spectral distortions (e.g., Kogut et al. 2011; Hernandez-Monteagudo et al. 2017). Recently, the first tentative detection of the integrated [CII] intensity at $z \sim 2.6$ was reported in Pullen et al. (2018) using Planck intensity maps cross-correlated with BOSS quasars and CMASS galaxies from SDSS-III. The main observable in a [CII] intensity mapping survey is the power spectrum of intensity fluctuations, $P_{\text{CII}}(k, z)$ as a function of scale and redshift. The astrophysical component of the power spectrum is encoded by the relation between the [CII] luminosity (which is used in computing the integrated emission intensity), and the underlying halo mass. Several theoretical and simulation approaches have been used to place constraints on this relation and the power spectrum of [CII] fluctuations up to the mid- to the end stages of reionization (e.g., Gong et al. 2012; Yue et al. 2015; Serra et al. 2016; Silva et al. 2015; Dumitru et al. 2018).

In this paper, we adopt a data-driven, halo model based approach to constraining the evolution of the [CII] luminosity - halo mass relation across redshifts with the help of the available data. We use the technique of abundance matching to derive constraints on the local [CII] luminosity - halo mass relation from the observations of the $z \sim 0$ [CII] luminosity function (Hemmati et al. 2017). We combine this information with the recent high-redshift constraints on the [CII] intensity (Pullen et al. 2018, assuming the CII detection) at $z \sim 2.6$ to model the evolution of this relation at higher redshifts, and find the predictions to be consistent with the currently available observational limits from galaxy data at $z \sim 4 - 6$ (Matsuda et al. 2015; Swinbank et al. 2012; Aravena et al. 2016). We use the [CII] luminosity - halo mass relation thus derived to calculate the power spectrum of intensity fluctuations across $z \sim 0 - 6$, and forecast its measurement sensitivity by future intensity mapping experiments.

The plan of the paper is as follows: In Sec. 2, we describe the current [CII] data used for constraining the model parameters and their evolution. We also describe the abundance matching procedure and the parameter constraints with their associated uncertainties. In the following section (Sec. 3), we use the resultant [CII] luminosity - halo mass relation to predict the power spectra of intensity fluctuations, both at low and high redshifts (up to $z \sim 6$). In Sec. 4, we use the results of the model with the parameters of several planned or upcoming [CII] intensity mapping experiments to place sensitivity forecasts on the expected [CII] auto-correlation signal. We summarize our results and discuss future prospects in Sec. 5. Throughout this work, we adopt a Λ CDM cosmology with the following parameters: $h = 0.71$, $\Omega_b = 0.046$, $\Omega_m = 0.281$, $\sigma_8 = 0.8$, $\Omega_\Lambda = 0.719$, $n_s = 0.963$.

2 MODELLING THE OCCUPATION OF CII

The main observable in [CII] intensity mapping is the power spectrum of fluctuations, denoted by $P_{\text{CII}}(k, z)$. This quantity is related to the intensity of the observed emission, given by:

$$I_{\nu, \text{CII}} = \frac{c}{4\pi} \int_0^\infty dz' \frac{\epsilon[\nu_{\text{obs}}(1+z')]}{H(z')(1+z')^4} \quad (1)$$

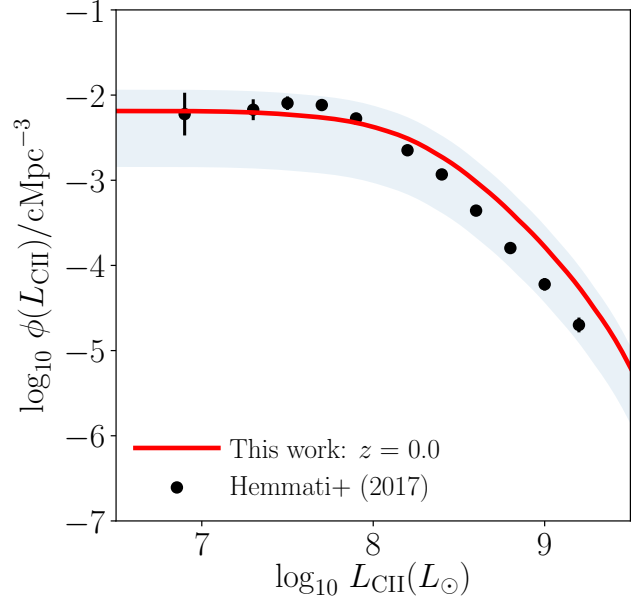


Figure 1. [CII] luminosity function at $z \sim 0$, along with the observational constraints (Hemmati et al. 2017) used in empirically deriving the $L_{\text{CII}} - M$ relation.

where the emissivity, $\epsilon(\nu)$ is given by:

$$\epsilon(\nu, z) = \delta_D(\nu - \nu_{\text{CII}})(1+z)^3 \int_{M_{\min, \text{CII}}}^\infty dM \frac{dn}{dM} L_{\text{CII}}(M, z) \quad (2)$$

where L_{CII} represents the luminosity of CII-emitting galaxies as a function of their halo mass M and redshift z , and $M_{\min, \text{CII}}$ stands for the minimum halo mass associated with CII-emitting galaxies. Thus the intensity of emission becomes:

$$I_{\nu, \text{CII}} = \frac{c}{4\pi} \frac{1}{\nu_{\text{CII}} H(z_{\text{CII}})} \int_{M_{\min, \text{CII}}}^\infty dM \frac{dn}{dM} L_{\text{CII}}(M, z) \quad (3)$$

The above expression thus depends on the relation between the [CII] luminosity and halo mass at different redshifts. Various approaches in the literature have been used to constrain this relation from hydrodynamical simulations and semi-analytical techniques. Here, we develop a data-driven, halo model framework for modelling this relation, following similar approaches for stellar-halo mass relations (e.g., Behroozi et al. 2013; Moster et al. 2013), the HI - halo mass relation (e.g., Padmanabhan & Refregier 2017; Padmanabhan & Kulkarni 2017; Padmanabhan et al. 2017) and the evolution of the CO luminosity - halo mass relation (e.g., Padmanabhan 2018).

The method outlined here relies on the technique of *abundance matching*, in which the relative abundances of [CII]-luminous galaxies and their associated host haloes are assumed to follow a one-to-one correspondence. In other words, the brightest [CII] emitting galaxies are assumed to populate the most massive dark matter haloes. This is equivalent to the assumption that:

$$\int_{M(L_{\text{CII}})}^\infty \frac{dn}{d \log_{10} M'} d \log_{10} M' = \int_{L_{\text{CII}}}^\infty \phi(L_{\text{CII}}) d \log_{10} L_{\text{CII}} \quad (4)$$

where $dn/d \log_{10} M$ is the number density of dark matter haloes with logarithmic masses between $\log_{10} M$ and $\log_{10}(M + dM)$,

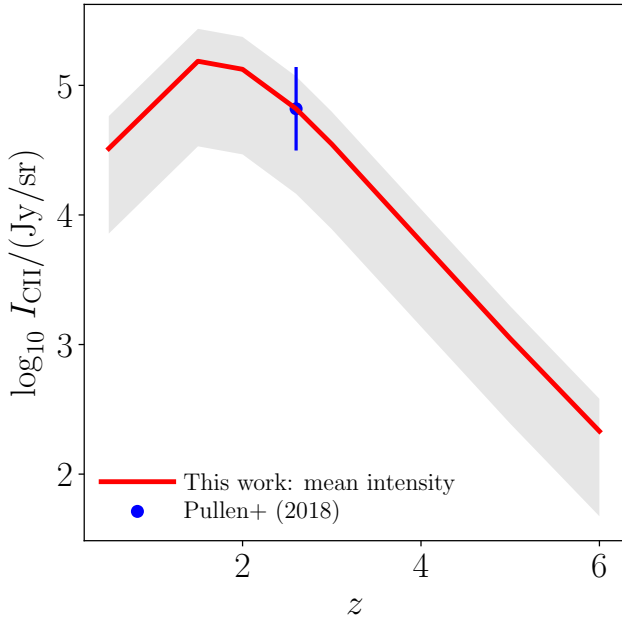


Figure 2. Evolution of mean intensity I_{CII} across redshifts from the best-fitting model parameters. Also shown is the intensity mapping constraint at $z \sim 2.6$ from the results of Pullen et al. (2018).

and $\phi(L_{\text{CII}})$ is the corresponding number density of [CII]-luminous galaxies in logarithmic luminosity bins.

At redshift zero, we use the recent available constraints on the local [CII] luminosity function observed with the Herschel PACS observations of the Luminous Infrared Galaxies in the Great Observatories All-sky LIRG Survey (Hemmati et al. 2017) to constrain the local [CII] luminosity - halo mass relation. Motivated by approaches to model the atomic hydrogen gas, in e.g., Padmanabhan et al. (2017), we use an $L_{\text{CII}} - M$ relation at $z \sim 0$ having a power law form with an exponential cutoff:

$$L_{\text{CII}}(M, z=0) = \left(\frac{M}{M_1}\right)^\beta \exp(-N_1/M) \quad (5)$$

with the three free parameters, M_1 , β and N_1 for the two characteristic mass scales and the slope of the relation.

We use the observed [CII] luminosity function [the raw data points in Hemmati et al. (2017)] abundance-matched to the Sheth-Tormen (Sheth & Tormen 2002) halo mass function in order to derive constraints on the parameters of the $L_{\text{CII}} - M$ relation from Equation (4). This gives the following best-fitting and error values for the free parameters:

$$\begin{aligned} M_1 &= (2.39 \pm 1.86) \times 10^{-5}; \quad N_1 = (4.19 \pm 3.27) \times 10^{11}; \\ \beta &= 0.49 \pm 0.38 \end{aligned} \quad (6)$$

Fig. 1 shows the luminosity function at $z \sim 0$ obtained from the best-fitting $L_{\text{CII}} - M$ relation thus obtained, and its associated uncertainty. Also shown are the data points from Hemmati et al. (2017) used in deriving this relation.

At high redshifts, the following datasets are available from candidate [CII] galaxies and blind searches:

(i) At $z \sim 4.4$, Swinbank et al. (2012) provide lower limits on the cumulative [CII] luminosity function based on observations of two ALMA candidate sub-millimetre galaxies (SMGs).

(ii) Matsuda et al. (2015) obtain upper limits on the cumulative [CII] luminosity function at $z \sim 4.5$, based on a blind search using ALMA archival data.

(iii) Aravena et al. (2016) obtain upper limits on the cumulative [CII] luminosity function at from the ASPECS blind survey $z \sim 6 - 8$ from candidate [CII]-emitters.

The first constraints on the integrated [CII] emission, $I_{\nu, \text{CII}}$ at $z \sim 2.6$ have been placed by Pullen et al. (2018) using cross-power spectra between high-frequency Planck intensity maps, spectroscopic quasars from BOSS-DR12 and CMASS galaxies from SDSS-III, finding a tentative [CII] intensity measurement of $I_{\nu, \text{CII}} = 6.6^{+5.0}_{-4.8} \times 10^4$ Jy/sr at 95% confidence.

To propagate the empirically derived $L_{\text{CII}} - M$ relation to higher redshifts, we use the observed evolution of the star formation rate density (SFRD; Madau & Dickinson 2014). This is consistent with the results of Hemmati et al. (2017), who find the observed [CII] luminosity function to evolve following that of the SFR (Behroozi et al. 2013), and Lagache et al. (2018) whose simulations do not find evidence for significant evolution in the $L_{\text{CII}} - \text{SFR}$ relation. The results of Pentericci et al. (2016) and Aravena et al. (2016) also find that the observations in the late stages of reionization closely follow the SFR-[CII] scaling, expressed in a power law form as $L_{\text{CII}} = \text{SFR}^\alpha$. Hence, the high- z [CII]-halo mass relation can be expressed as :

$$L_{\text{CII}}(M, z) = \left(\frac{M}{M_1}\right)^\beta \exp(-N_1/M) \left(\frac{(1+z)^{2.7}}{1 + [(1+z)/2.9]^{5.6}}\right)^\alpha \quad (7)$$

The value of α is constrained by fitting the intensity mapping measurement of Pullen et al. (2018) at $z \sim 2.6$ using Eq. (3).³ This leads to $\alpha = 1.79 \pm 0.30$; the intensity mapping data may favor values consistent with (though slightly higher than) those predicted by the simulations of Lagache et al. (2018). The present data do not constrain a mass-dependent redshift evolution of the $L_{\text{CII}} - M$ relation, but only the component arising from the evolution of the star formation rate density.⁴ The data also do not constrain the redshift evolution of the parameter α itself, though several studies report the values for different galaxy samples across redshifts (e.g., De Looze et al. 2011). Such a redshift dependence may also be suggested by the results of simulations (Lagache et al. 2018).

Keeping in mind that the present study does not consider instrumental systematic effects or foreground contamination, the quoted errors are conservative estimates: the fitting errors are added in quadrature to the observational uncertainties from Hemmati et al. (2017) for the case of $z \sim 0$. For the high- z parameters, the upper and lower limits of the Pullen et al. (2018) measurement are used along with the fitting errors to estimate the parameter uncertainties.

The predicted evolution of the mean intensity of [CII] emission, $I_{\nu, \text{CII}}$ across redshifts is shown in Fig. 2 along with the data

³ This measurement is also sensitive to the minimum halo mass $M_{\text{min}, \text{CII}}$ used in the calculation of $I_{\nu, \text{CII}}$. Throughout this work, we use $M_{\text{min}, \text{CII}} = 10^{10} h^{-1} M_\odot$ for consistency, which also gives a good fit to the intensity mapping data for sensible values of the evolution parameter α .

⁴ Note that this makes the implicit assumption that the SFRD is separable, i.e. $\text{SFR}(M, z) = f(M)g(z)$. Although this separability may not be strictly true in general, this functional form is found to provide a good fit to the available [CII] data (and is also supported by the fact that the [CII] luminosity functions thus derived closely resemble those from semi-analytic models invoking more detailed sub-grid treatments of SFR and ISM physics across redshifts, e.g., in Fig. 3).

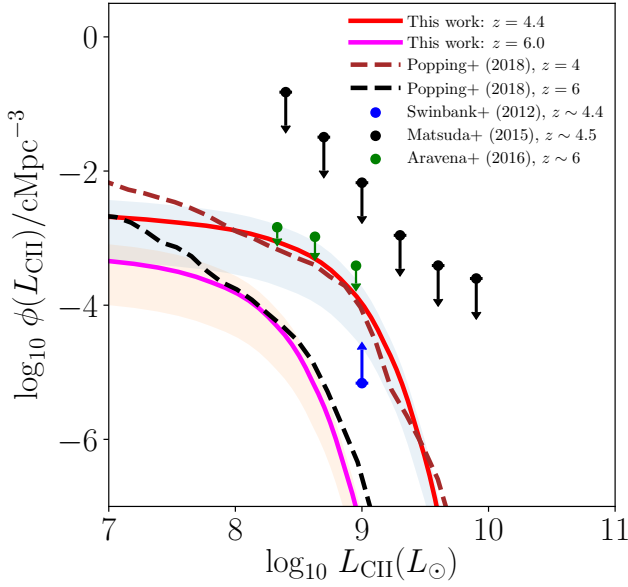


Figure 3. [CII] luminosity function from the best-fitting model at higher redshifts ($z \sim 4.4$ and $z \sim 6$), along with the currently available limits at $z \sim 4.4$ (Swinbank et al. 2012; Matsuda et al. 2015) and $z \sim 6$ (Aravena et al. 2016). Also shown are the results from the semi-analytic modelling of Popping et al. (2018) at $z \sim 4$ and $z \sim 6$.

point at $z \sim 2.6$ from Pullen et al. (2018). The resultant $L_{\text{CII}} - M$ relation is also found to be consistent with the limits from the observations (Matsuda et al. 2015; Swinbank et al. 2012; Aravena et al. 2016) at higher redshifts $z \sim 4 - 6$, as shown in Fig. 3. Also shown are the results from the semi-analytical modelling of Popping et al. (2018) at $z \sim 4$ and $z \sim 6$, which uses a sub-grid treatment of SFR and ISM physics across redshifts.

3 RESULTANT [CII]-HALO MASS RELATION AND POWER SPECTRUM

The [CII] luminosity - halo mass relation from the present data can thus be described by the functional form in Eq. (7), with the best-fitting parameters:

$$M_1 = (2.39 \pm 1.86) \times 10^{-5}; N_1 = (4.19 \pm 3.27) \times 10^{11}; \\ \beta = 0.49 \pm 0.38; \alpha = 1.79 \pm 0.30 \quad (8)$$

The relation for redshifts 0.5, 1.5, 5 and 6 is plotted on the panels of Fig. 4 along with the estimated uncertainties (shown by the grey bands⁵). These can now be used to derive the predicted [CII] power spectrum of intensity fluctuations using the relations:

$$P_{\text{shot}}(z) = \frac{\int_{M_{\text{min,CII}}}^{\infty} dM (dn/dM) L_{\text{CII}}(M, z)^2}{\left(\int_{M_{\text{min,CII}}}^{\infty} dM (dn/dM) L_{\text{CII}}(M, z) \right)^2} \quad (9)$$

⁵ The maximum relative errors in the fitted parameters are used to derive conservative uncertainty estimates for the $L_{\text{CII}} - M$ relation and power spectrum. Possible uncertainties in the $M_{\text{min,CII}}$ parameter are not folded into the present estimates.

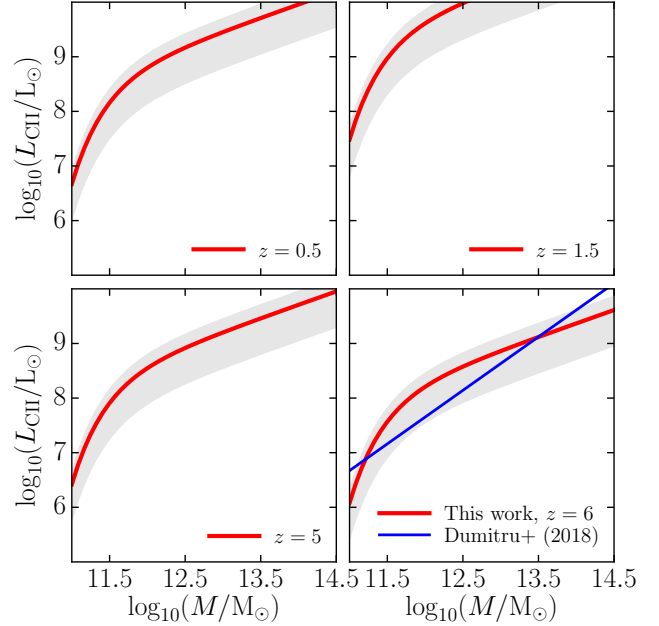


Figure 4. The $L_{\text{CII}} - M$ relation for $z = 0.5, 1.5, 5$ and 6 from the best-fitting model. The associated uncertainties are shown by the grey bands. The $L_{\text{CII}} - M$ relation from the simulations of Dumitru et al. (2018) is overplotted at $z \sim 6$ for comparison.

representing the shot noise component, and

$$b_{\text{CII}}(z) = \frac{\int_{M_{\text{min,CII}}}^{\infty} dM (dn/dM) L_{\text{CII}}(M, z) b(M, z)}{\int_{M_{\text{min,CII}}}^{\infty} dM (dn/dM) L_{\text{CII}}(M, z)} \quad (10)$$

representing the clustering. In the above expression, $b(M, z)$ denotes the dark matter halo bias following Scoccimarro et al. (2001). These can be combined to obtain the full power spectrum:

$$P_{\text{CII}}(k, z) = I_{\nu, \text{CII}}(z)^2 [b_{\text{CII}}(z)^2 P_{\text{lin}}(k, z) + P_{\text{shot}}(z)] \quad (11)$$

The power spectra of intensity fluctuations thus derived are plotted for $z = \{0.5, 1.5, 5, 6\}$ in the panels of Figs. 5 and 6, in units of $(\text{Jy/sr})^2$. Also plotted for the higher redshift panels are the semi-empirical and simulation estimates for the same redshifts obtained in the literature:

(i) Visbal & Loeb (2010) present an analytical formalism to calculate the cross-correlation power spectra for different emission lines including OI, OII, OIII, NII and CO transitions.

(ii) Gong et al. (2012) obtain the [CII] line intensity fluctuations over $z \sim 6 - 8$ by modelling the various radiative processes in the ISM both analytically and numerically.

(iii) Silva et al. (2015) use four different models, m1, m2, m3 and m4 corresponding to different parameterizations of the [CII] luminosity to SFR relation coupled to results from simulations.

(iv) Serra et al. (2016) present a framework based on measurements of the cosmic infrared background (CIB) to compute the intensity mapping power spectra of multiple far infra-red cooling lines in the ISM, including [CII], [NII], [OI] and the CO transitions.

Although there is considerable variation in the power spectra values in the literature, we note that the predicted values are also sensitive to the choice of the parameter $M_{\text{min,CII}}$ as discussed

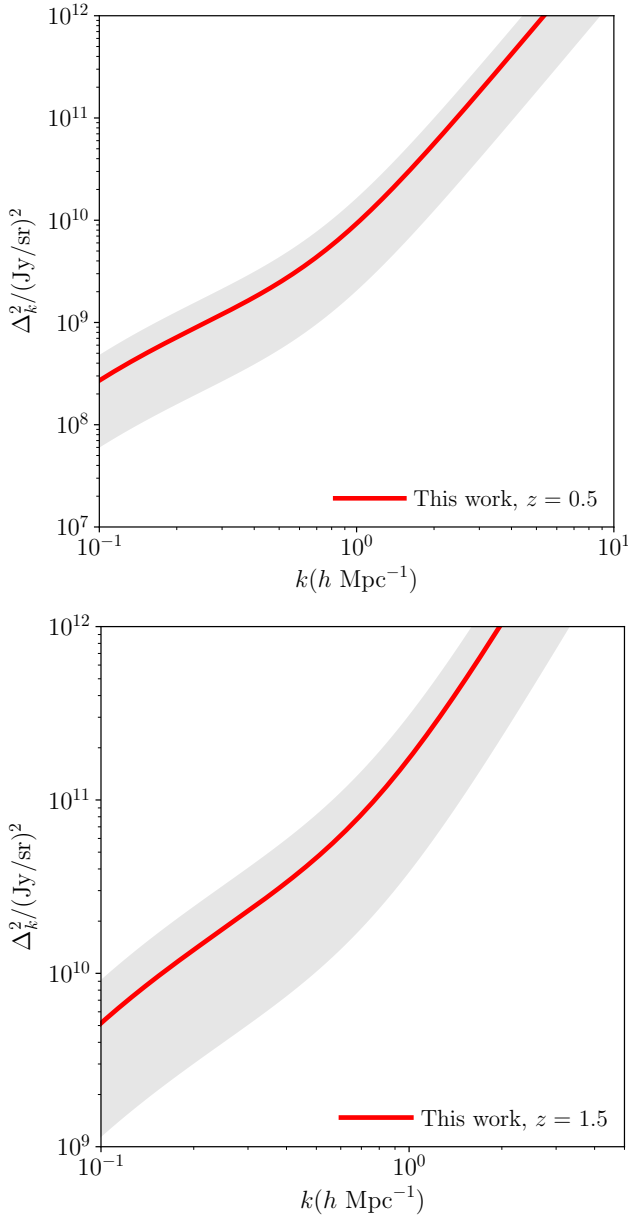


Figure 5. [CII] intensity power spectra at $z \sim 0.5, 1.5$ from the empirical relation. The associated uncertainties are shown by the grey bands.

in the previous section. Nevertheless, these plots provide an estimate of the effect of the intensity mapping measurement, if confirmed, on the sensitivities of future [CII] measurements at post-reionization epochs. We explore this more fully in the following section.

4 SENSITIVITY FORECASTS

In this section, we use the predicted evolution of the power spectra of [CII] intensity fluctuations to place constraints on the SNR expected from current and future experiments targeting [CII] over post-reionization epochs. We consider configurations resembling the following [CII] experiments in this work, with parameters as provided in Table 1:

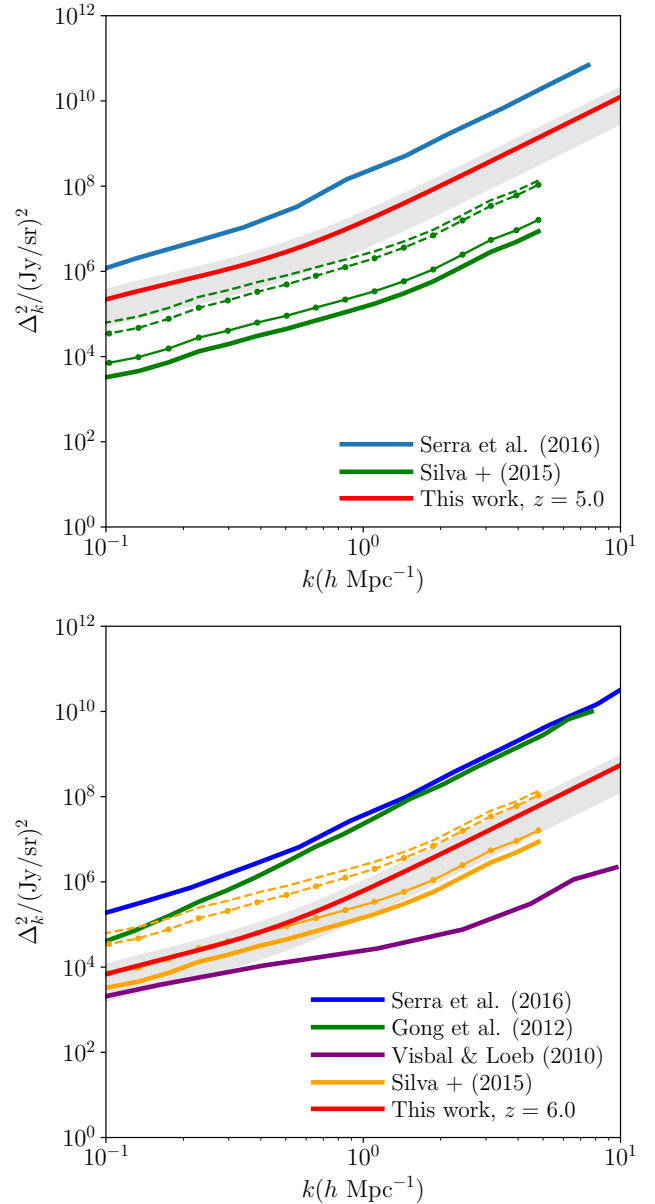


Figure 6. [CII] intensity power spectra at $z \sim 5, 6$ from the present work compared to other model and simulation predictions from the literature, from Serra et al. (2016); Gong et al. (2012); Visbal & Loeb (2010); Silva et al. (2015). Note that the Silva et al. (2015) models are for $z \sim 6.7$. The different linestyles for the Silva et al. (2015) denote the four different models m1, m2, m3 and m4 in that work.

(i) A Primordial Inflation Explorer (PIXIE; Kogut et al. 2011, 2014)-like mission which aims to measure spectral distortions of the CMB over a broad range of frequencies. This experiment will be able to detect [CII] intensity fluctuations at $z \sim 0.05 - 11.7$, and is suitable for wide field intensity mapping surveys, including in cross-correlation with galaxy data (e.g., Uzgil et al. 2014; Switzer 2017; Pullen et al. 2018). This survey can be assumed to cover the full sky area (E. Switzer, private communication); we restrict to 2π sr, corresponding to about 20000 deg² in order to avoid the Galactic plane.

(ii) An upcoming Spectroscopic Terahertz Airborne Receiver

for Far-InfraRed Exploration (STARFIRE; Aguirre 2015; Hailey-Dunsheath et al. 2018)⁶-like experiment, a balloon-borne, far-infrared spectroscopic array with tomographic sensitivity to [CII] over $z \sim 0.5 - 1.6$, planned to be hosted on a 2.5 m aperture telescope.

(iii) An EXperiment for Cryogenic Large-Aperture Intensity Mapping (EXCLAIM)-like configuration (E. Switzer and A. Pullen, private communication) for CO and [CII] at redshifts $z \sim 3$, to be hosted on a 0.74 m aperture telescope.

(iv) The CONCERTO experiment aims to map CII evolution over $z \sim 4.5 - 8.5$ using the 12-m APEX telescope at Chajnantor in Chile (Lagache et al. 2018; Serra et al. 2016). Parameters for a CONCERTO-like configuration are based largely on the recent analysis of Dumitru et al. (2018).

(v) A Tomographic Intensity Mapping Experiment (TIME; Crites et al. 2017)-like configuration which aims to measure the [CII] line intensity emission over the redshift range $5 < z < 9$. We consider a survey area of $78'$ by $0.5'$ with a 12-m aperture telescope, and other parameters of the TIME-Pilot experiment following the discussions in Crites et al. (2014).

(vi) The Cerro Chajnantor Atacama Telescope (CCAT)-prime experiment (Parshley et al. 2018) with the Prime-Cam instrument (Vavagiakis et al. 2018) and P-Spec imaging spectrometer, plans to probe the late stages of reionization using [CII] line emission over $z \sim 5 - 8$. The parameters adopted for a CCAT-p-like configuration are based on the discussions in the document, https://www.ccatobservatory.org/docs/pdfs/Draft_CCAT-p_prospectus.170809.pdf.

(vii) Finally, we consider a [CII] intensity mapping survey with the ALMA telescope (e.g. Carilli et al. 2018) based on the ALMACAL experiment (e.g., Klitsch et al. 2018) targeting [CII] line emission over $z \sim 5 - 9$. Such surveys have been discussed, e.g., in the context of the ALMA Spectroscopic Survey in the Hubble Deep Field (ASPECS; Walter et al. 2014; Carilli et al. 2016). The parameters used here correspond to a survey using the ALMA array over 1000 hours of observation targeting 5 arcmin^2 .

For each experiment, we calculate the noise power spectrum using the following equations (Silva et al. 2015; Serra et al. 2016; Dumitru et al. 2018):

$$P_N = V_{\text{pix}} \frac{\sigma_N^2}{t_{\text{pix}}} \quad (12)$$

We now consider the terms in the RHS of the above Eq. (12) one by one. The time per observing pixel, t_{pix} is given by:

$$t_{\text{pix}} = t_{\text{obs}} N_{\text{spec,eff}} \frac{\Omega_{\text{beam}}}{S_A} \quad (13)$$

In the above expression, t_{obs} is the total observing time, S_A is the survey area, $\Omega_{\text{beam}} = 2\pi\sigma_{\text{beam}}^2$, with $\sigma_{\text{beam}} = \theta_{\text{beam}}/2.355$ in terms of the beam angular size θ_{beam} . The beam FWHM is calculated using the diffraction formula $\theta_{\text{beam}} = 1.22\lambda_{\text{obs}}/D_{\text{dish}}$, where $\lambda_{\text{obs}} = 158 \mu\text{m}(1+z)$ for all the experiments except the PIXIE-like configuration. For PIXIE, we assume a FWHM of 1.65 deg due to the detectors being highly multi-moded (Switzer 2017, and E. Switzer, private communication). $N_{\text{spec,eff}}$ is the effective number of detectors which integrate in parallel on voxels on a given frequency.

The pixel volume, V_{pix} is given by (Gong et al. 2012; Dumitru

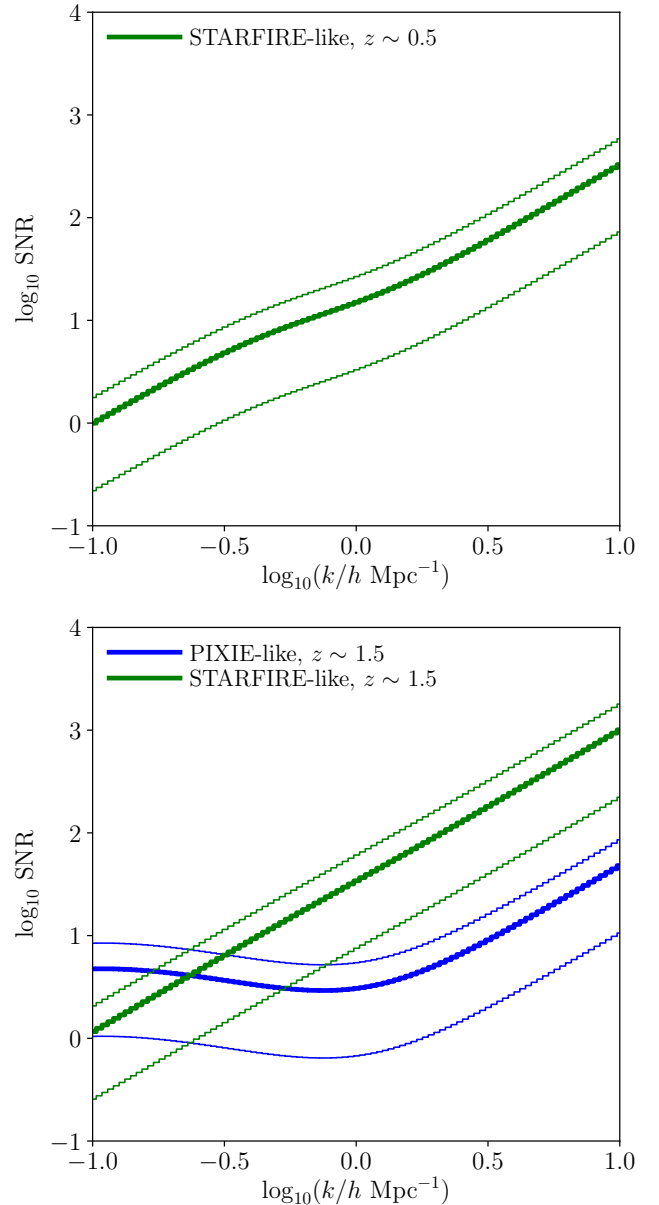


Figure 7. Signal-to-noise ratios at $z \sim 0.5$ (top panel) and $z \sim 1.5$ (lower panel) from the empirical relation and the parameters of the PIXIE- and STARFIRE-like configurations. The associated uncertainties in the mean value of the signal are indicated by the thinner steps.

et al. 2018):

$$V_{\text{pix}} = 1.1 \times 10^3 (\text{cMpc}/h)^3 \left(\frac{\lambda}{158 \mu\text{m}} \right) \left(\frac{1+z}{8} \right)^{1/2} \left(\frac{\theta_{\text{beam}}}{10'} \right)^2 \left(\frac{\Delta\nu}{400\text{MHz}} \right) \quad (14)$$

as a function of the rest wavelength λ of the line transition, the redshift z and the spectral resolution $\Delta\nu$.

The variance per pixel, σ_N in Eq. (12) is given by:

$$\sigma_N = \frac{\text{NEFD}}{\Omega_{\text{beam}}} \quad (15)$$

where the NEFD (Noise Equivalent Flux Density), can be calcu-

⁶ <https://asd.gsfc.nasa.gov/conferences/FIR/posters/Aguirre.STARFIRE.pdf>

Configuration	D_{dish} (m.)	$\Delta\nu$ (MHz)	$N_{\text{spec,eff}}$	S_A (sq. deg.)	NEFD (mJy $s^{1/2}$) / σ_N (Jy $s^{1/2}$ / sr)	B_ν (GHz)	t_{surv} (h.)
PIXIE-like	0.55 [†]	15000	4	20000	5.83×10^6 [†]	120	1500
STARFIRE-like	2.5	1700	100	1	2.6×10^7 [†]	15	450
EXCLAIM-like	0.74	1000	6	400	6×10^5 [†]	120	8
CONCERTO-like	12	1500	1500	1.4	155	40	1200
TIME-like	12	400	32	0.01	65	40	1000
CCAT-p-like	6	400	200	16	2.5×10^6 [†]	40	4000
ALMACAL-like *	12	15	3000	0.0014	2.85*	8	1000

Table 1. Various experimental configurations considered in this work. [†]: A FWHM of 1.65 deg is used as a good approximation for the PIXIE-like configuration (Switzer 2017) instead of the usual diffraction formula, due to the detectors being highly multi-moded. For the PIXIE-like, STARFIRE-like, EXCLAIM-like and CCAT-p-like configurations, the value of σ_N is directly quoted in units of Jy $s^{1/2}$ / sr; for all other experiments, the value of the NEFD is quoted in mJy $s^{1/2}$. For PIXIE, the σ_N is calculated from Eq. (15) assuming the NEP value 0.7×10^{-16} W/ $\sqrt{\text{Hz}}$ and the etendu of 4 cm² sr from Kogut et al. (2011). For the STARFIRE-like experiment, the median value of σ_N from the experiment description in https://asd.gsfc.nasa.gov/conferences/FIR/posters/Aguirre_STARFIRE.pdf is used. *For the ALMA intensity mapping survey considered here, we use an ALMACAL-like configuration targeting [CII] in Band 6. The NEFD is calculated from the rms sensitivity in a field, which is taken to be roughly $S_{\text{rms}} = 0.09$ mJy on combining 30 pointings.

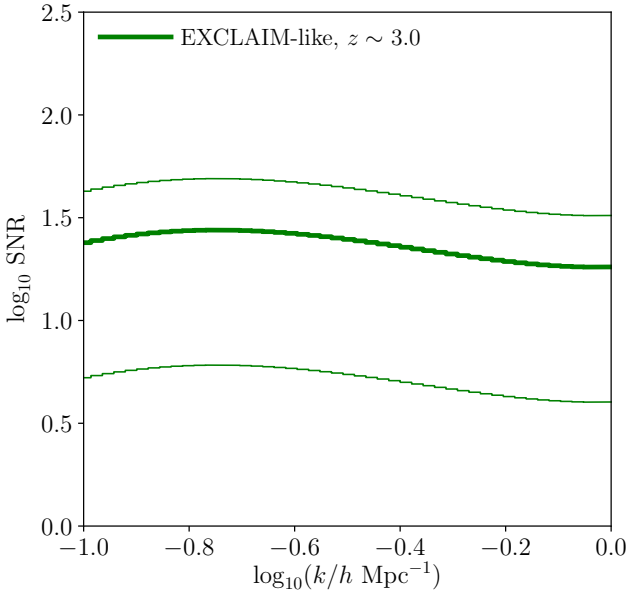


Figure 8. Signal-to-noise ratio at $z \sim 3$ from the empirical relation and the parameters of the EXCLAIM-like configuration. The associated uncertainties in the mean value of the signal are indicated by the thinner steps.

lated on the sky for the instrument under consideration by using the expression:

$$\text{NEFD} = \frac{\text{NEI}}{\sqrt{N_{\text{detectors}}}} \quad (16)$$

where the NEI is the Noise Equivalent Intensity (in units of Jy $s^{1/2}$ /sr) and represents the intensity required to achieve a signal-to-noise ratio of unity at the detector, and $N_{\text{detectors}}$ is the number of detectors.⁷

For the ALMACAL-like configuration, the survey considered

⁷ For some experiments, the value of the Noise Equivalent Power (NEP) is quoted instead of the NEI; the NEI is then calculated by using $\text{NEI} \approx \text{NEP}/\text{etendu}$ where the etendu $A_{\text{det}}\Omega_{\text{beam}}$ is the product of the detector area A_{det} and the detector solid angle Ω_{beam} .

targets [CII] in Band 6 using four 2 GHz windows. The NEFD = $S_{\text{rms}}t_{\text{int}}^{1/2}$ is calculated from the integration time $t_{\text{int}} = 1000$ hours and the rms sensitivity S_{rms} in a field, which is taken to be roughly $S_{\text{rms}} = 0.09$ mJy on combining 30 pointings for this survey.⁸ The $N_{\text{spec,eff}}$ here corresponds to the number of spatial resolution elements, which is close to 3000 for the full survey area (R. Dutta and T. Mroczkowski, private communication).

Once the noise power is known, the variance of the [CII] observation is calculated as:

$$\text{var}_{\text{CII}} = \frac{(P_{\text{CII}} + P_N)^2}{N_{\text{modes}}} \quad (17)$$

with the number of modes given by:

$$N_{\text{modes}} = 2\pi k^2 \Delta k \frac{V_{\text{surv}}}{(2\pi)^3} \quad (18)$$

with Δk denoting the bin width in k -space (for all the experiments considered here, we use logarithmically equispaced k -bins with $\Delta \ln k = 0.05$), and the survey volume (Gong et al. 2012; Dumitru et al. 2018) given by:

$$V_{\text{surv}} = 3.7 \times 10^7 (\text{cMpc}/h)^3 \left(\frac{\lambda}{158 \mu\text{m}} \right) \left(\frac{1+z}{8} \right)^{1/2} \left(\frac{S_A}{16 \text{deg}^2} \right) \left(\frac{B_\nu}{20 \text{GHz}} \right) \quad (19)$$

Finally, the SNR is calculated from Eq. (17) as:

$$\text{SNR} = \frac{P_{\text{CII}}}{(\text{var}_{\text{CII}})^{1/2}} \quad (20)$$

for each experiment under consideration.

The SNRs for surveys with the seven experiments described above and in Table 1 are plotted in the panels of Figs. 7, 8 and 9 respectively. As the sensitivity depends on the assumed k -bin size (Δk) through the number of modes (Eq. (18)), the SNRs for each experimental configuration are plotted as stair steps in $\log-k$ space. The associated signal uncertainties are indicated by the thinner steps in each case. Note that the SNRs derived here may be somewhat optimistic since the derivation above does not take

⁸ Note that the product of $t_{\text{int}}^{1/2}$ and S_{rms} remains constant given a particular configuration.

into account the beam and spectral width transfer functions. Specifically, SNR estimates beyond $k \sim 1 \text{ Mpc}^{-1}$ may be subject to caveats coming from beam size in some configurations.⁹

To illustrate the scaling of the SNR with the parameters of the experimental configurations, we consider the examples of the CONCERTO-like and CCAT-p-like cases at $z \sim 6$. From Eqs. (13) and (14), we have:

$$\frac{V_{\text{pix}}}{t_{\text{pix}}} \propto \frac{\Delta\nu S_A}{t_{\text{obs}} N_{\text{spec,eff}}} \quad (21)$$

and hence (using Table 1):

$$\left(\frac{V_{\text{pix}}}{t_{\text{pix}}} \right)_{\text{concerto}} / \left(\frac{V_{\text{pix}}}{t_{\text{pix}}} \right)_{\text{ccatp}} = 0.15 \quad (22)$$

Using Eq. (15) to calculate σ_N for the CONCERTO-like case at $z \sim 6$, we find:

$$(\sigma_N^2)_{\text{concerto}} / (\sigma_N^2)_{\text{ccatp}} \sim 18.72 \quad (23)$$

which places the noise powers (P_N 's) for the CONCERTO-like and CCAT-p-like configurations roughly a factor 2.81 apart.

Noting from Eq. (19) that $V_{\text{surv}} \propto B_\nu S_A$, we find that

$$(V_{\text{surv}})_{\text{concerto}} / (V_{\text{surv}})_{\text{ccatp}} = 0.0875 \quad (24)$$

which can be used in Eq. (18) to calculate the ratio of N_{modes} .

When both the CONCERTO-like and CCAT-p-like surveys are in their noise dominated regimes, this leads to the required ratio of the SNRs:

$$\text{SNR}_{\text{ccatp}} / \text{SNR}_{\text{concerto}} \sim 9.50 \quad (25)$$

This is illustrated in the lower panel of Fig. 9, which shows the mean SNRs of the CONCERTO-like and CCAT-p-like configurations spaced roughly an order of magnitude apart, at a typical scale of $k \sim 1$ where both are noise dominated.¹⁰

The ‘turnover’ scale of the SNR at which a survey switches from being noise-dominated to sample variance (or cosmic variance) dominated occurs when $P_{\text{CII}} > P_N$ in Eq. (17). This is relevant for configurations with smaller survey areas, e.g., in the ALMACAL-like configuration, the SNR at $z \sim 5 - 6$ (where $P_{\text{CII}} \gg P_N$) is essentially a function of the survey volume throughout the k -range considered here: $\text{SNR} = N_{\text{modes}}^{1/2}$. This also occurs in the STARFIRE-like case at $z \sim 1.5$ where the [CII] signal is much larger than the noise term.

5 CONCLUSIONS

We have developed a data-driven, halo model based framework towards interpreting future intensity mapping experiments involving

⁹ Chung et al. (2018b) adopt a more sophisticated line-scan survey strategy for TIME, finding a combined SNR across $k \lesssim 1$ to be of order unity at $z \sim 6$. Noting that the water vapour levels at the telescope site considered in that work lead to an equivalent NEFD of about 100 (D. Chung, private communication), the SNR values here are consistent with Chung et al. (2018b) to within an order of magnitude.

¹⁰ For the CONCERTO-like experiment, we find the SNR at $z \sim 6$ to be of order a few around $k \lesssim 1$, which is roughly consistent with the results of Dumitru et al. (2018), noting that our model predictions in Fig. 6 around $z \sim 6$ are close to those in Dumitru et al. (2018, Fig. 3 top panel). Note that we assume in this case (D. Chung and G. Lagache, private communication) that the configuration uses 1500 pixels per array (one for 200–360 GHz and one for 125–300 GHz).

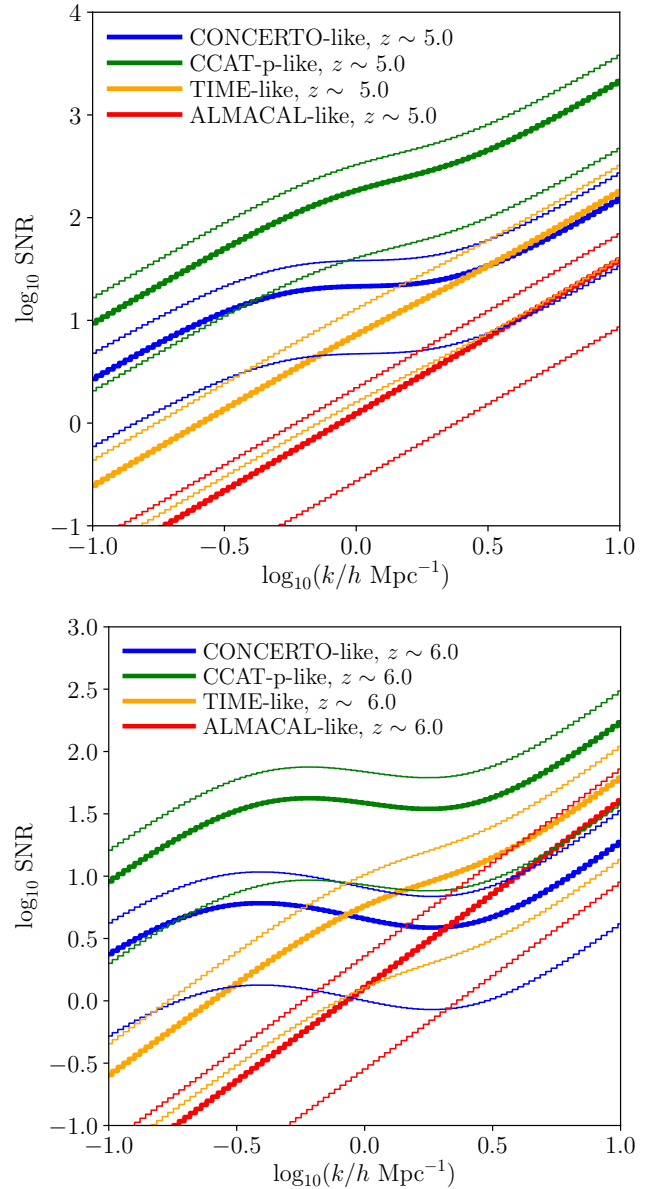


Figure 9. Signal-to-noise ratios at $z \sim 5$ (top panel) and $z \sim 6$ (lower panel) from the empirical relation and the parameters of four future [CII] experiments: with the CCAT-p-like, CONCERTO-like, TIME-like and ALMACAL-like intensity mapping configurations. The associated uncertainties in the mean value of the signal are indicated by the thinner steps.

the ionized carbon (CII) emission with rest-wavelength $158 \mu\text{m}$. Combining data from low redshift galaxy survey constraints (Hemmati et al. 2017) on the [CII] luminosity function, the empirical evolution of the star-formation rate density (Madau & Dickinson 2014) and the high-redshift constraints from the recent intensity mapping experiment at $z \sim 2.6$ (Pullen et al. 2018, assuming the CII detection), we develop fitting forms for the local [CII] luminosity - halo mass relation and its predicted evolution with redshift. Although the current data at higher redshifts mainly provide upper or lower limits to the [CII] luminosity function, the predicted evolution is fully consistent with these constraints. This formalism is used to predict the power spectra of [CII] intensity fluctuations both

at intermediate redshifts as well as towards the end stages of reionization. The best-fitting model and the parametrisation are summarized in Table 2.

As indicated in Pullen et al. (2018), a confirmation of this initial [CII] intensity mapping measurement would provide exciting insights for galaxy evolution and the metallicity of the ISM. From the results of the present work, we find that it can also be used to investigate how the [CII] - SFRD relation evolves with redshift during and after the peak of star formation in the universe. An assumption implicit in the present model is that the [CII]-SFRD connection continues to hold up to $z \sim 6$ representing the end stages of reionization. This is supported by the recent findings of Smit et al. (2018) who find no evidence for a deviation in the mean [CII] luminosity - SFR relation at $z \sim 6.8$ (compared to $z \sim 0$ and $z \sim 5.5$ galaxies) from ALMA observations of [OIII] - selected galaxies; however, at higher redshifts ($z \sim 7$), other results (Pentericci et al. 2016) suggest a deficit in the [CII] luminosity compared to the lower redshift CII - SFR relation in Ly- α selected CII galaxies. Clearly, further constraints on this dependency would be possible with the present model in conjunction with future [CII] surveys in the late stages of the reionization phase of the universe. Larger, homogeneous CII galaxy detections would also help place independent constraints on the evolution of the slope of the [CII] - SFRD relation, thus helping confirm the robustness of the intensity mapping measurements. Extrapolating this dependence to even higher redshifts would be possible with the data from blind or dedicated surveys with the JWST/ALMA.

The present work does not examine the effects of foregrounds, which would presumably be the limiting systematic in [CII] surveys at reionization epochs. The most dominant interloper lines arise from the CO (3-2) and (4-3) emission from $z \sim 0 - 2$, with an additional component coming from the cosmic infrared background (CIB). Efficient removal techniques (cleaning/masking) have been developed to mitigate line foregrounds (e.g., Breyse et al. 2015; Cheng et al. 2016; Visbal & Loeb 2010; Lidz & Taylor 2016; Sun et al. 2018). At lower redshifts, the main contaminants are expected to be Galactic and extragalactic thermal dust emissions and their associated instrument response. However, at these frequencies, the results of simulations indicate excellent prospects for the robust recovery of the [CII] signal by using linear combination cleaning techniques (e.g., Switzer 2017).

It is of interest to explore cross-correlation possibilities with [CII] intensity mapping and large galaxy photometric/spectroscopic redshift surveys to be undertaken in the future, which would provide valuable information about the stellar and gas properties of dark matter haloes. Such cross-correlation studies in the context of CO (e.g., Chung et al. 2018a) may promise good constraints on the astrophysical parameters of the CO luminosity - halo mass relation and would offer interesting complementary information in the case of [CII], especially in the context of planned surveys with several future programs, e.g. the forthcoming ALPINE survey¹¹ which aims to measure [CII] properties in a sample of galaxies between $4 < z < 6$. Cross-correlations of galaxy survey data with [CII] intensity maps can also be used to shed light into various processes of galaxy formation and the metal enrichment of the ISM. Through the mid to end stages of reionization, synergies with HI and other surveys can offer exciting prospects into constraints on cosmology and astrophysics, including the baryon cycle and star formation rate, as well as the predicted sizes of ionization

Table 2. Summary of the best-fitting $L_{\text{CII}} - M$ relation, and the free parameters involved. The L_{CII} is in units of L_{\odot} and all masses are in units of M_{\odot} .

$L_{\text{CII}}(M, z) = F(z)[(M/M_1)^\beta \exp(-N_1/M)];$	
$F(z) = ((1+z)^{2.7}/(1+[(1+z)/2.9]^{5.6}))^\alpha$	
$M_1 = (2.39 \pm 1.86) \times 10^{-5};$	
$N_1 = (4.19 \pm 3.27) \times 10^{11} M_{\odot};$	
$\alpha = 1.79 \pm 0.30$	
$\beta = 0.49 \pm 0.38$	

bubbles from the turnover of the cross-correlation coefficient (Visbal & Loeb 2010; Gong et al. 2012; Dumitru et al. 2018).

ACKNOWLEDGEMENTS

I thank Marco Viero, Girish Kulkarni, Dongwoo Chung, Guochao Sun, Marta Silva, Patrick Breyse and Guilaine Lagache for helpful initial conversations and discussions related to [CII] intensity mapping. I thank Martin Zwaan, Gergö Popping, Fabian Walter, Celine Peroux, Rajeshwari Dutta and Tony Mroczkowski for useful discussions especially regarding possible ALMA intensity mapping surveys, and the ESO, Garching and the MPIA, Heidelberg for hospitality during my visits. I thank Simon Foreman, Anthony Pullen, Christos Karoumpis and José Fonseca for detailed comments on the manuscript. I am grateful to Marta Silva, Sebastian Dumitru and Gergö Popping for sharing data from their simulations. It is a pleasure to thank Dongwoo Chung for a very careful reading of the manuscript, several useful comments and for sharing a draft version of his work in preparation. I thank the referee for a helpful report that improved the presentation of the paper. I also thank Guilaine Lagache, Eric Switzer, Celine Peroux and Tony Mroczkowski for helpful inputs regarding the various instrumental and survey designs used. My research was supported by the Tomalla Foundation.

REFERENCES

- Aguirre J., 2015, The Spectroscopic Terahertz Airborne Receiver for Far-Infrared Exploration (STARFIRE): a Next-Generation Experiment for Galaxy Evolution Studies, NASA APRA Proposal
- Anderson C. J., et al., 2018, *MNRAS*, **476**, 3382
- Aravena M., et al., 2016, *ApJ*, **833**, 71
- Behroozi P. S., Wechsler R. H., Conroy C., 2013, *ApJ*, **770**, 57
- Breyse P. C., Kovetz E. D., Kamionkowski M., 2015, *MNRAS*, **452**, 3408
- Capak P. L., et al., 2015, *Nature*, **522**, 455
- Carilli C. L., et al., 2016, *ApJ*, **833**, 73
- Carilli C. L., Murphy E. J., Ferrara A., Dayal P., 2018, preprint, ([arXiv:1810.07536](https://arxiv.org/abs/1810.07536))
- Chang T.-C., Pen U.-L., Bandura K., Peterson J. B., 2010, *Nature*, **466**, 463
- Cheng Y.-T., Chang T.-C., Bock J., Bradford C. M., Cooray A., 2016, *ApJ*, **832**, 165
- Chung D. T., et al., 2018a, preprint, ([arXiv:1809.04550](https://arxiv.org/abs/1809.04550))
- Chung D. T., Viero M. P., Church S. E., Wechsler R. H., 2018b, arXiv e-prints, [p. arXiv:1812.08135](https://arxiv.org/abs/1812.08135)

¹¹ <http://cosmos.astro.caltech.edu/page/submm#>

- Crites A. T., et al., 2014, in *Millimeter, Submillimeter, and Far-Infrared Detectors and Instrumentation for Astronomy VII*. p. 91531W, [doi:10.1117/12.2057207](#)
- Crites A., et al., 2017, in *American Astronomical Society Meeting Abstracts* #229. p. 125.01
- De Looze I., Baes M., Bendo G. J., Cortese L., Fritz J., 2011, *MNRAS*, **416**, 2712
- De Looze I., et al., 2014, *A&A*, **568**, A62
- Dumitru S., Kulkarni G., Lagache G., Haehnelt M. G., 2018, preprint, ([arXiv:1802.04804](#))
- Fonseca J., Maartens R., Santos M. G., 2018, *MNRAS*, **479**, 3490
- Gong Y., Cooray A., Silva M., Santos M. G., Bock J., Bradford C. M., Zemcov M., 2012, *ApJ*, **745**, 49
- Hailey-Dunsheath S., et al., 2018, *Journal of Low Temperature Physics*, Hemmati S., Yan L., Diaz-Santos T., Armus L., Capak P., Faisst A., Masters D., 2017, *ApJ*, **834**, 36
- Hernandez-Monteagudo C., Maio U., Ciardi B., Sunyaev R. A., 2017, preprint, ([arXiv:1707.01910](#))
- Klitsch A., Péroux C., Zwaan M. A., Smail I., Oteo I., Biggs A. D., Popping G., Swinbank A. M., 2018, *MNRAS*, **475**, 492
- Kogut A., et al., 2011, *J. Cosmology Astropart. Phys.*, **7**, 025
- Kogut A., et al., 2014, in *Space Telescopes and Instrumentation 2014: Optical, Infrared, and Millimeter Wave*. p. 91431E, [doi:10.1117/12.2056840](#)
- Lagache G., 2018, in Jelić V., van der Hulst T., eds, *IAU Symposium Vol. 333, Peering towards Cosmic Dawn*. pp 228–233 ([arXiv:1801.08054](#)), [doi:10.1017/S1743921318000558](#)
- Lagache G., Cousin M., Chatzikos M., 2018, *A&A*, **609**, A130
- Li T. Y., Wechsler R. H., Devaraj K., Church S. E., 2016, *ApJ*, **817**, 169
- Lidz A., Taylor J., 2016, *ApJ*, **825**, 143
- Madau P., Dickinson M., 2014, *ARA&A*, **52**, 415
- Mashian N., Sternberg A., Loeb A., 2015, *J. Cosmology Astropart. Phys.*, **11**, 028
- Masui K. W., et al., 2013, *ApJ*, **763**, L20
- Matsuda Y., Nagao T., Iono D., Hatsukade B., Kohno K., Tamura Y., Yamaguchi Y., Shimizu I., 2015, *MNRAS*, **451**, 1141
- Moradinezhad Dizgah A., Keating G. K., 2018, preprint, ([arXiv:1810.02850](#))
- Moster B. P., Naab T., White S. D. M., 2013, *MNRAS*, **428**, 3121
- Padmanabhan H., 2018, *MNRAS*, **475**, 1477
- Padmanabhan H., Kulkarni G., 2017, *MNRAS*, **470**, 340
- Padmanabhan H., Refregier A., 2017, *MNRAS*, **464**, 4008
- Padmanabhan H., Refregier A., Amara A., 2017, *MNRAS*, **469**, 2323
- Parshley S. C., et al., 2018, in *Society of Photo-Optical Instrumentation Engineers (SPIE) Conference Series*. p. 107005X ([arXiv:1807.06675](#)), [doi:10.1117/12.2314046](#)
- Pentericci L., et al., 2016, *ApJ*, **829**, L11
- Popping G., Narayanan D., Somerville R. S., Faisst A. L., Krumholz M. R., 2018, preprint, ([arXiv:1805.11093](#))
- Pullen A. R., Serra P., Chang T.-C., Doré O., Ho S., 2018, *MNRAS*, **478**, 1911
- Scoccamarro R., Sheth R. K., Hui L., Jain B., 2001, *ApJ*, **546**, 20
- Serra P., Doré O., Lagache G., 2016, *ApJ*, **833**, 153
- Sheth R. K., Tormen G., 2002, *MNRAS*, **329**, 61
- Silva M., Santos M. G., Cooray A., Gong Y., 2015, *ApJ*, **806**, 209
- Smit R., et al., 2018, *Nature*, **553**, 178
- Sun G., et al., 2018, *ApJ*, **856**, 107
- Swinbank M., et al., 2012, *The Messenger*, **149**, 40
- Switzer E. R., 2017, *ApJ*, **838**, 82
- Switzer E. R., et al., 2013, *MNRAS*, **434**, L46
- Uzgil B. D., Aguirre J. E., Bradford C. M., Lidz A., 2014, *ApJ*, **793**, 116
- Vavagiakis E. M., et al., 2018, in *Society of Photo-Optical Instrumentation Engineers (SPIE) Conference Series*. p. 107081U ([arXiv:1807.00058](#)), [doi:10.1117/12.2313868](#)
- Visbal E., Loeb A., 2010, *J. Cosmology Astropart. Phys.*, **11**, 016
- Walter F., et al., 2014, *ApJ*, **782**, 79
- Yue B., Ferrara A., Pallottini A., Gallerani S., Vallini L., 2015, *MNRAS*, **450**, 3829